Ultracompact Dual-Polarized Cross-Dipole Antenna for 5G Base Station Array of Low Wind Load

Biying Han [1], Qi Wu [1], Chen Yu [1], Haiming Wang [2], Xiqi Gao [1], and Ni Ma [1]

[1]Affiliation not available
[2]Southeast University

October 30, 2023

Abstract

Very high wind loads represent one of the major problems for the ultralarge-scale 5G base station array at the sub-6 GHz band, where dozens of or hundreds of antennas are used. An ultracompact dual-polarized cross-dipole antenna with an extremely small overall projected area is presented. The array with low wind load is realized by miniaturized cross dipoles and the replacement of the traditional ground plane with a defected ground structure (DGS) and metal mesh reflector. The DGS is utilized to realize size reduction and isolation enhancement. The projected area of the antenna is reduced by 70%. Therefore, each antenna in the array can be independently packaged using a streamlined radome with a low wind load. And the inter-radome spacing is large enough to make holes that are used to further reduce wind load. The antenna prototype is designed, fabricated, and measured for the sub-1 GHz band. The measured results show that the impedance bandwidth is 680-970 MHz, the polarization isolation is higher than 20 dB, and the gain is around 6.5 dBi. It is verified that the proposed ultracompact antenna of high radiation performance is very suitable for an ultralarge-scale array of low wind load in a 5G base station.

Ultracompact Dual-Polarized Cross-Dipole Antenna for 5G Base Station Array of Low Wind Load

Biying Han, *Student Member, IEEE*, Qi Wu, *Member, IEEE*, Chen Yu, *Member, IEEE*, Haiming Wang, *Member, IEEE*, Xiqi Gao, *Fellow, IEEE*, and Ni Ma, *Senior Member, IEEE*

***Abstract*—Very high wind loads represent one of the major problems for the ultralarge-scale 5G base station array at the sub-6 GHz band, where dozens of or hundreds of antennas are used. An ultracompact dual-polarized cross-dipole antenna with an extremely small overall projected area is presented. The array with low wind load is realized by miniaturized cross dipoles and the replacement of the traditional ground plane with a defected ground structure (DGS) and metal mesh reflector. The DGS is utilized to realize size reduction and isolation enhancement. The projected area of the antenna is reduced by 70%. Therefore, each antenna in the array can be independently packaged using a streamlined radome with a low wind load. And the inter-radome spacing is large enough to make holes that are used to further reduce wind load. The antenna prototype is designed, fabricated, and measured for the sub-1 GHz band. The measured results show that the impedance bandwidth is 680–970 MHz, the polarization isolation is higher than 20 dB, and the gain is around 6.5 dBi. It is verified that the proposed ultracompact antenna of high radiation performance is very suitable for an ultralarge-scale array of low wind load in a 5G base station.**

***Index Terms*—Base station antennas, antenna miniaturization, dual-polarization, cross-dipole antenna, defected ground structure (DGS), low wind load.**

I. INTRODUCTION

MASSIVE multiple-input multiple-output (mMIMO) technology uses numerous transmit and receive antennas to provide many more degrees of freedom in the spatial domain and to increase spectral efficiency [1]. The fifth-generation (5G) mobile communication system provides high data rates, low latency, and significant capacity improvement using this mMIMO technology [2], [3]. In the 5G era, main-stream base station sites have evolved into the form of a baseband unit (BBU) plus an active antenna unit (AAU). The high requirements on the performance of mMIMO lead to a sharp increase in the number of base station antennas, which negatively affects the production and installation of AAUs. Wind load occurs because of the AAU area. Increasing the number of antennas means a higher capacity but a larger projected area for AAUs, which results in a high wind load for AAUs in the sub-6 GHz band. And this problem becomes more severe especially for AAUs in the sub-1 GHz band [4].

To date, research on the wind load of antennas has mainly focused on aircraft antennas, large reflector antennas and large deep space observatory antennas [5]–[9]. However, as the number of base station antennas increases to hundreds and even more than a thousand in 5G and beyond systems, the influence of wind load on ultralarge-scale antenna arrays cannot be ignored. In other words, wind load is one of the key performance indicators for ultralarge-scale antenna arrays and is also one of the key constraints on increasing the number of base station antennas. The influence of wind load on large antennas operating under open-air atmospheres was studied in [8], [9]. Through the analysis and simulation of antenna deflection and deformation caused by wind load, a compensation algorithm for the control center that dynamically adjusted the antenna was proposed, thereby reducing the detection error. However, this compensation algorithm cannot reduce the wind load of a large antenna. According to [4], there are three aspects that can determine the wind load of the antenna: the force coefficient, the projected area and the dynamic pressure. The force coefficient is decided by the shape of the antenna; the projected area is the size of the windward side, which depends on the wind direction and the size of the antenna; and the dynamic pressure is a square function of the wind velocity and cannot be changed artificially. An aircraft antenna with a saber-like structure was proposed to reduce wind load by reducing the cross-section in front, giving it a small projected area [5]–[7]. Additionally, this kind of saber antenna has a shape that is conducive to airflow, resulting in a further reduction in the wind load.

From the discussion above, it is obvious that reducing the projected area of the base station antenna is the most effective and convenient method for achieving a low wind load. Moreover, it is necessary to simultaneously consider both the aerodynamic aspects (projected area, wind load, etc.) and the electromagnetic aspects (reflection coefficient, isolation between different input ports, realized gain, cross-polarization

Manuscript received Nov. 23, 2021; revised , 2021; accepted . Date of publication ; date of current . This work was supported in part by the National Key R&D Program of China under Grant 2020YFB1804901, the National Natural Science Foundation of China under Grants 62001101 and 61960206006, the Science Foundation of Jiangsu Province under Grant BK20200349, and the Huawei Cooperation Project. Part of this work has been published in Proceedings of 2021 IEEE/CIC International Conference on Communications in China (ICCC Workshops). *(Corresponding author: Haiming Wang.)*

B. Y. Han, Q. Wu, C. Yu, and H. M. Wang are with the State Key Laboratory of Millimeter Waves, Southeast University, Nanjing 210096, China, and also with the Purple Mountain Laboratories, Nanjing 211100, China (e-mail: byhan@seu.edu.cn, qiwu@seu.edu.cn, chenyu@seu.edu.cn, hmwang@seu.edu.cn).

X. Q. Gao is with the National Mobile Communications Research Laboratory, Southeast University, Nanjing 210096, China and also with the Purple Mountain Laboratories, Nanjing 211100, China (e-mail: xqgao@seu.edu.cn).

N. Ma is with the Huawei Technologies Co., Ltd., Shenzhen 518129, China (e-mail: ni.ma@huawei.com).

Color versions of one or more of the figures in this paper are available online at http://ieeexplore.ieee.org.

Digital Object Identifier

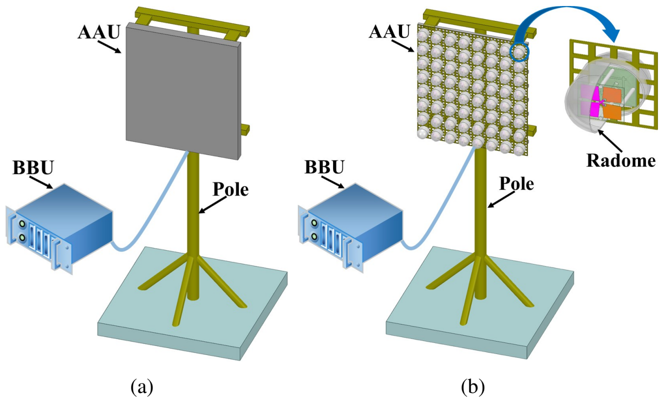

Fig. 1. Conceptual prototypes of (a) a traditional AAU and (b) an AAU with low wind load.

level, etc.).

Considering the traditional structure of antenna elements, the projected area is mostly determined by the size of the metal ground of the antenna array. A conceptual prototype of a traditional AAU operating in the sub-1 GHz band is shown in Fig. 1(a). It uses one radome to protect all antenna elements and RF modules, increasing the projected area, especially when there are a large number of antenna elements. It is necessary to change the intact metal ground structure to achieve a small projected area. A ventilated base station antenna array is a feasible and effective method for dramatically reducing the projected area. Fig. 1(b) presents a conceptual prototype of a novel AAU with a ventilated metal ground. Streamlined small radomes installed on the metal mesh can be utilized to separately protect the antenna element and its RF module, tremendously reducing the overall projected area and achieving a low wind load. Moreover, the lightweight metal mesh reduces the requirements for installation poles.

To increase the ventilation area as much as possible, antenna miniaturization research is of great significance. However, traditional compact antenna design mainly focuses on reducing the size of the radiating part of the antenna. To realize a low wind load for base station antennas, a compact antenna structure must be a small radiator and have a small overall projected area. Previous research on compact antennas still has important reference value.

Over the past years, various research methods have been proposed to achieve antenna miniaturization. Through the innovation of the radiating structure, a compact antenna structure can be accomplished. Sharing some common structures, cutting some noncritical boards [10], applying fractal-shaped radiators [11], [12], etching DGSs on the ground [13], [14], and implementing half of the driven loop element of the radiating part on each side of the substrate [15] can reduce the size of antennas. For folded patch antennas, antenna miniaturization can be facilitated by loading innovative slots (interdigitated slots [16], multiple C-shaped slotlines [17], etc.) to replace the original standard straight slot, which shifts the resonance condition to a lower operating band. Folded dipole antennas can also be utilized to generate new resonant modes, providing a compact antenna structure and enhanced bandwidth [18]. Moreover, a compact dual-polarized cross-dipole antenna was proposed in [19]. Size reduction was realized by installing parasitic elements and optimizing the shape of crossed dipoles.

Recently, metamaterials have been utilized to simultaneously reduce the size of antennas and enhance radiation performance [20]–[23]. In [20], owing to the increase in the effective permeability of the substrate in the presence of metamaterials, metamaterial loading was proposed to miniaturize an antenna without much compromise from the impedance and radiation characteristics. [21] proposed a compact planar antenna by utilizing metamaterial unit cells on the reflector element, which made the antenna operate at lower frequencies without the need to increase its physical size. Moreover, reflector elements loaded with metamaterial units can be utilized to reduce the profile height of an antenna [23]. However, compact antennas with metamaterials usually have complicated structures and high costs, which is not appropriate for large-scale processes and production.

In this work, a compact $\pm 45^\circ$ dual-polarized cross-dipole antenna [24] with an extremely small overall projected area is presented for a 5G base station antenna array with low wind load [25]. The overall projected area reduction is realized by loading a defected ground structure (DGS) on the ground layer to enhance the S-parameters and replacing the traditional metal ground with a metal mesh reflector [26]. The DGS on the ground layer extends the path of the surface current and generates a continuous current strip, reducing the coupling between the two input ports. The metal mesh reflector enhances the radiation performance of the proposed antenna while reducing the overall projected area. The major contributions of this work are listed as follows:

1) The proposed antenna is mainly for reducing the wind load of the base station array, which is of great significance, especially for base stations operating in the 5G low/mid band.
2) A dual-polarized cross-dipole antenna with an extremely small projected area is proposed. Each antenna in the array can be independently packaged using a streamlined radome with a low wind load. And the inter-radome spacing is large enough to make holes that are used to further reduce wind load.
3) A DGS layer and metal mesh reflector are combined to replace the traditional metal ground plane of the cross-dipole antenna, which enables the ultralarge-scale antenna array to realize a low wind load and to maintain high-radiation performance characteristics.

The rest of this paper is organized as follows. The design of a low wind load antenna is presented in Section II. Experimental results and discussion are shown in Section III. Section IV concludes this article.

II. Antenna Design

A. Compact Low Wind Load Antenna

The proposed compact antenna with a low wind load is shown in Fig. 2. This antenna with an extremely small projected area consists of a radiating layer, defected ground layer,

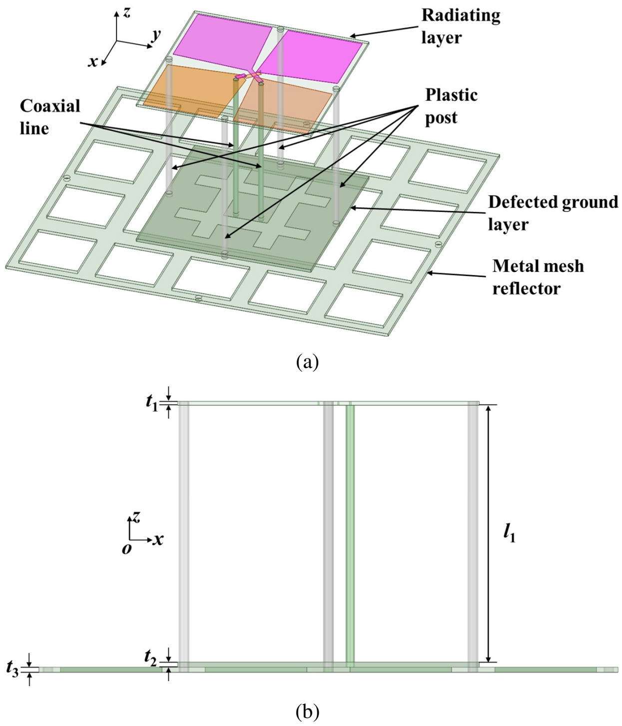

Fig. 2. Configuration of the proposed compact antenna with and extremely small projected area: (a) three-dimensional view and (b) side view.

TABLE I
GEOMETRIC PARAMETERS OF THE LOW WIND LOAD ANTENNA

Parameter	t_1	t_2	t_3	l_1	h
Value (mm)	1.524	2.0	2.0	101.0	40.88
Parameter	d	s_1	s_2	s_3	a
Value (mm)	5.0	11.59	88.83	20.75	40.0
Parameter	w_1	w_2	w_3	w_4	w_5
Value (mm)	109.72	118.72	3.42	260.0	228.0

metal mesh reflector, coaxial lines and plastic posts. More details about the radiating layer, defected ground layer and metal mesh reflector are given in Fig. 3. The radiating layer consists of two pairs of vertical bow-tie dipoles to achieve $\pm 45°$ polarization. As shown in Fig. 3(a), each pair of bow-tie dipoles is printed on the front side and back side of the Taconic RF-35 substrate. The substrate has a dielectric constant of 3.5 and thickness of $t_1 = 1.524$ mm. A 50-Ohm microstrip stub is utilized to excite a pair of bow-tie dipoles. One side of the stub is connected to one half of the dipole printed on the front side, and the other side of the stub is connected to the inner conductor of the coaxial line [27]. Note that to avoid the cross-connection of two stubs, part of the stub of the $-45°$ polarized dipole is printed on the back side of the substrate and connected together by two metallic holes. Additionally, the outer conductor of the coaxial line is soldered on half of the bow-tie dipole printed on the back side of the substrate. The coaxial line at port 1 excites the $+45°$ polarized dipole, and the coaxial line at port 2 excites the $-45°$ polarized dipole.

The defected ground layer shown in Fig. 3(b) is constructed using a printed circuit board (PCB) process. The DGS is

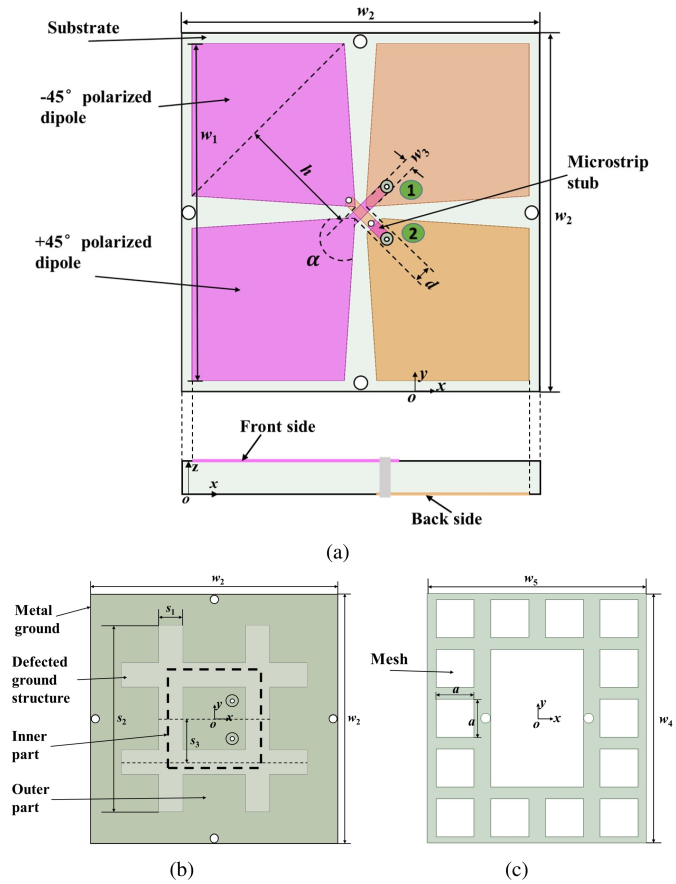

Fig. 3. Geometry of the presented radiating layer, defected ground layer and metal mesh reflector: (a) top view and side view of the radiating layer, (b) top view of the defected ground layer and (c) top view of the metal mesh reflector.

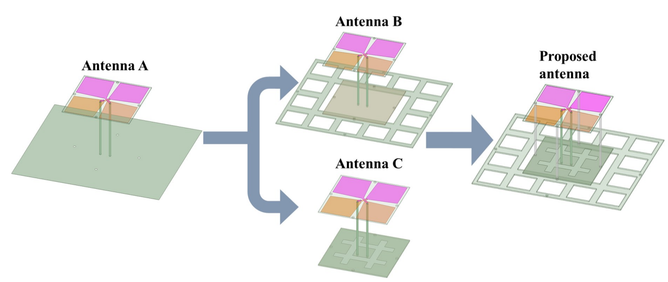

Fig. 4. Transformation from the traditional cross-dipole antenna to the proposed low wind load antenna.

printed on an FR4 substrate with a dielectric constant of 4.4 and thickness of $t_2 = 2.0$ mm. Two horizontal slots and two vertical slots intersect perpendicularly, forming the DGS. The inner part surrounded by these four slots is connected with the outer conductor of the coaxial lines, and the outer part is separate from the inner part; this can be regarded as a parasitic patch. To maintain the stability of the physical structure of the proposed antenna, the DGS is printed on the FR4 substrate instead of by direct etching on the metal ground.

The traditional metal ground is replaced by the defected layer and the metal mesh reflector presented in Fig. 3(c) to reduce the overall projected area, and the middle part of the metal mesh reflector is removed so that coaxial lines can be

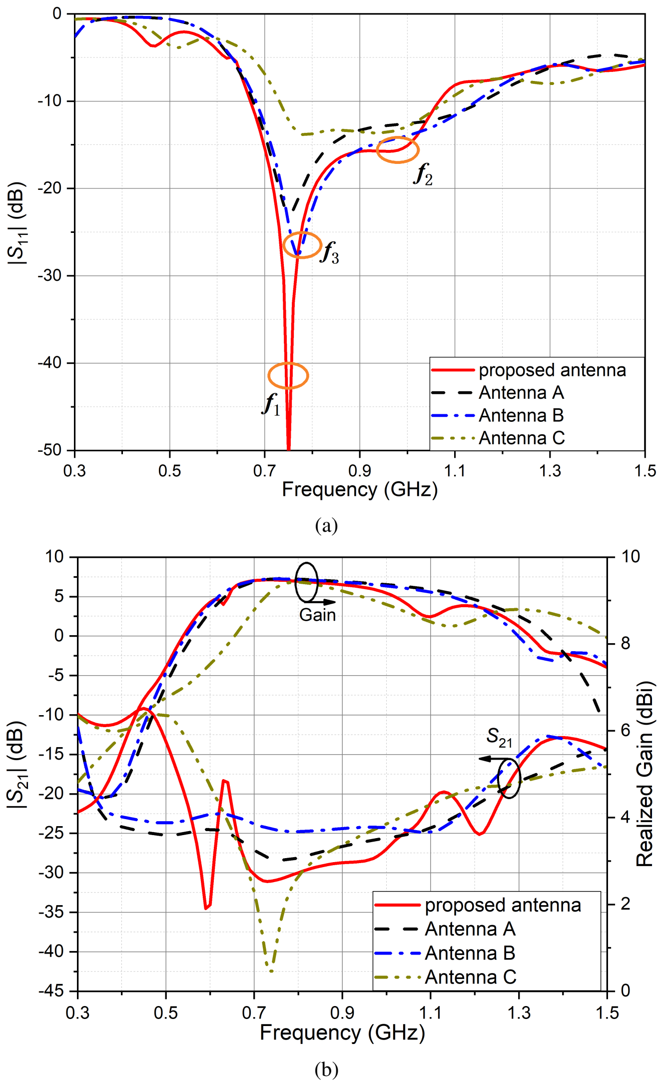

Fig. 5. Simulated (a) reflection coefficients, (b) isolation between two input ports and realized gains of dual-polarized cross-dipole antennas with different structures.

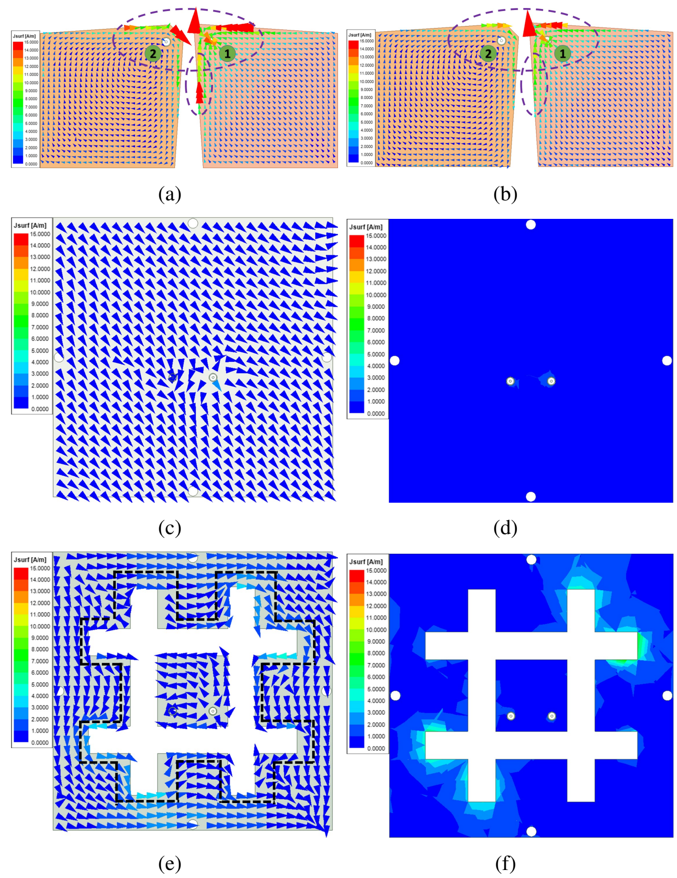

Fig. 6. Surface current distribution on half of the dipole printed on the back side of the substrate of (a) Antenna B at 750 MHz and (b) the proposed antenna at 750 MHz. Surface current distribution on the cut metal ground of Antenna B at (c) 750 MHz and (d) 980 MHz. Surface current distribution on the defected ground layer of the proposed antenna at (e) 750 MHz and (f) 980 MHz.

more conveniently installed. Four plastic posts with diameters of 4 mm are utilized to support the proposed antenna. The key dimensions of the low wind load antenna are presented in Table I.

Fig. 4 shows the transformation from the traditional cross-dipole antenna to the proposed antenna. The radiating parts of these different antennas have the same reduction in size. The simulated S-parameters and gains for different structures are given in Fig. 5. The traditional $\pm 45°$ dual-polarized cross-dipole antenna with an intact metal ground (Antenna A) refers to the antenna proposed in [27]. Additionally, the geometry of the radiator is changed, the size of the radiating part is reduced, and the metal ground is connected with the outer conductor of the coaxial lines. The purpose of this work is to propose a low wind load antenna that can not only reduce the projected area but also meet or surpass the radiation performance of the traditional antenna with an intact metal ground. To reduce the overall projected area, a cross-dipole antenna with a cut metal ground and metal mesh reflector (Antenna B) is presented, and the cut metal ground is the same size as the radiating part.

From Fig. 5, it can be seen that the reflection coefficient and realized gain for Antenna B are similar to those for Antenna A, which indicates that the metal mesh reflector has the ability to maintain radiating characteristics while the projected area is reduced. However, the isolation between the two input ports of Antenna B deteriorates. From 670-690 MHz, the reflection coefficient for these two structures performs poorly owing to the smaller radiating part. The S-parameters for Antenna B need further improvement.

To improve the S-parameters for the structures with the traditional metal ground or cut metal ground, a defected ground layer is proposed in this work. A cross-dipole antenna with a defected ground layer (Antenna C) is then presented. Fig. 5(b) shows that the isolation between the two input ports of Antenna C has been enhanced at lower operating frequencies. However, the realized gain of Antenna C shown in Fig. 5(b) is quite undesirable in working frequencies. The radiation produced by the defected ground layer introduces negative effects in the higher frequency band.

It is clear that simply loading the defected ground layer makes the realized gain decrease sharply in the operating frequencies, and simply using a cut metal ground with a metal mesh reflector cannot meet the requirements of the S-

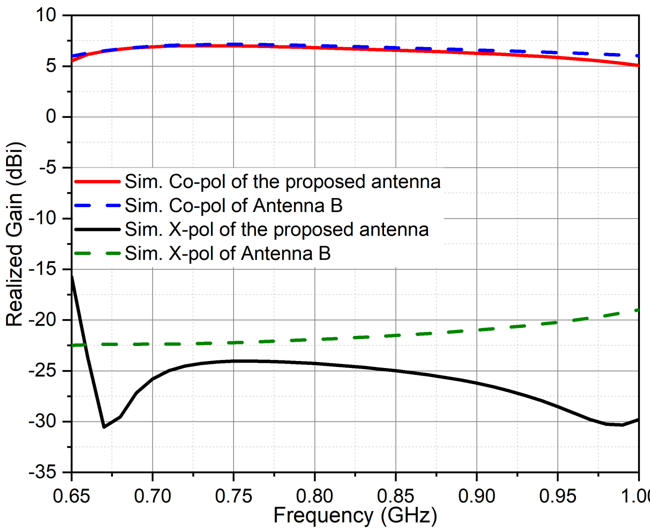

Fig. 7. Simulated normal gains of the proposed antenna and Antenna B when port 1 is excited.

parameters at lower working frequencies. Under these circumstances, a cross-dipole antenna with a defected ground layer and metal mesh reflector is proposed to simultaneously reduce the projected area and achieve preferable radiation characteristics.

As shown in Fig. 5(a), compared with Antenna B, which has only one resonance frequency f_3, the proposed antenna has two resonance frequencies, f_1 and f_2, and resonance frequency f_1 is lower than resonance frequency f_3. To present the influence of the DGS on the S-parameters, the surface current distributions of both Antenna B and the proposed antenna are compared in Fig. 6. From Fig. 6(d) and Fig. 6(f), it can be seen that when the proposed antenna works at 980 MHz, there is an obvious current distribution around the slots and on the outer parasitic patch of the proposed antenna, in contrast to Antenna B. This means that most of the energy is stored and that there is no outgoing radiation, which explains the generation of resonance frequency f_2 by the proposed antenna. Resonance frequency f_2 improves the reflection coefficient at higher working frequencies.

Moreover, when port 1 is excited, a comparison of the surface current distribution shown in Fig. 6(a) and Fig. 6(b) clearly shows that the surface current around two input ports is changed due to the DGS layer, especially as marked by the purple dotted lines. As shown in Figs. 6(c) and 6(e), when the DGS layer is used, the current flowing around port 2 will flow along the outer conductor of the coaxial line and then flow along the continuous current strip forming by four perpendicularly intersecting slots. In this case, the magnitude of the surface current around port 2 is reduced, which can weaken negative influence on port 1 and reduce coupling between two ports. Consequently, the isolation between the two input ports is improved. The isolation enhancement can also be proved by the simulated normal gains of the proposed antenna and Antenna B. As shown in Fig. 7, from 680 MHz to 970 MHz, the simulated cross-polarization level of the proposed antenna is lower than that of Antenna B owing to

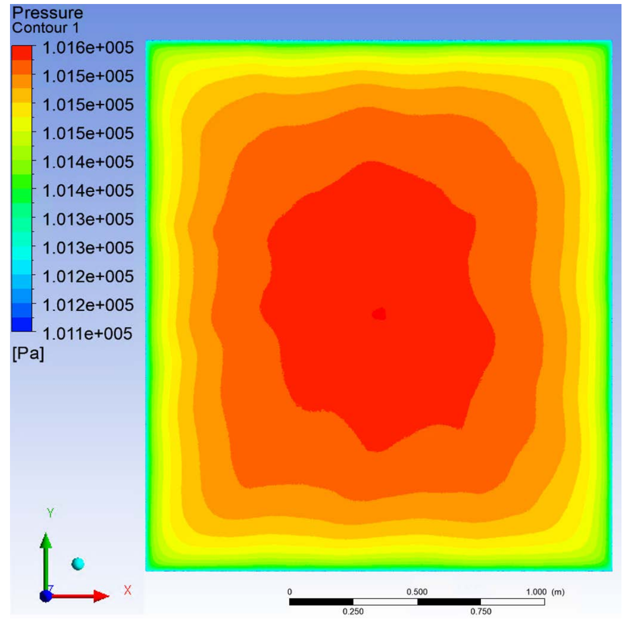

(a)

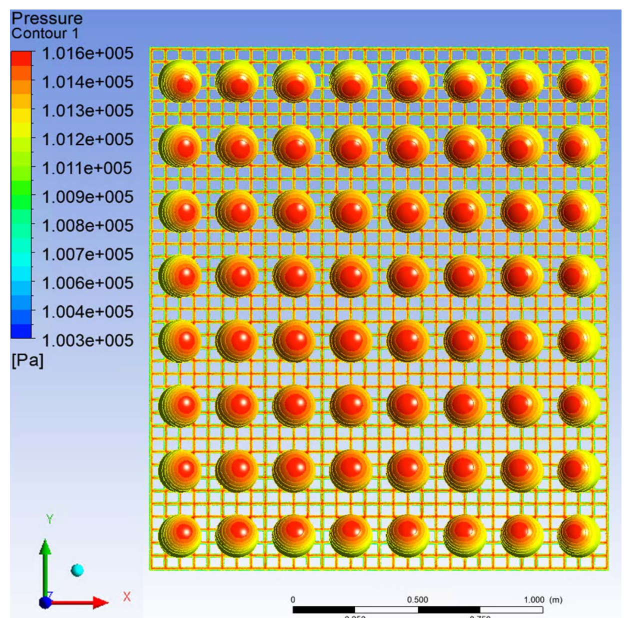

(b)

Fig. 8. Simulated wind load for the prototypes of (a) the traditional 64-element AAU and (b) low wind load AAU.

the reduced coupling between the two input ports.

Furthermore, as marked by the black dotted lines, the new surface current path along the four loaded slots also makes the electrical length a bit more longer than that of Antenna B. Therefore, the resonance frequency f_1 is lower than the resonance frequency f_3, which increases the impedance bandwidth at low frequencies. Additionally, a comparison of the reflection coefficients of Antenna C and the proposed antenna shows that the metal mesh reflector placed right behind the defected ground layer can further extend the surface current path while maintaining the realized gain and reducing the projected area, which improves the reflection performance.

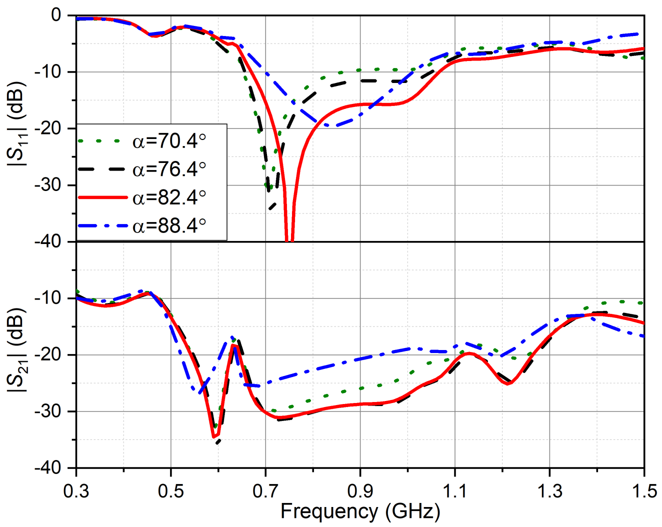

Fig. 9. S-parameters of the proposed antenna versus α.

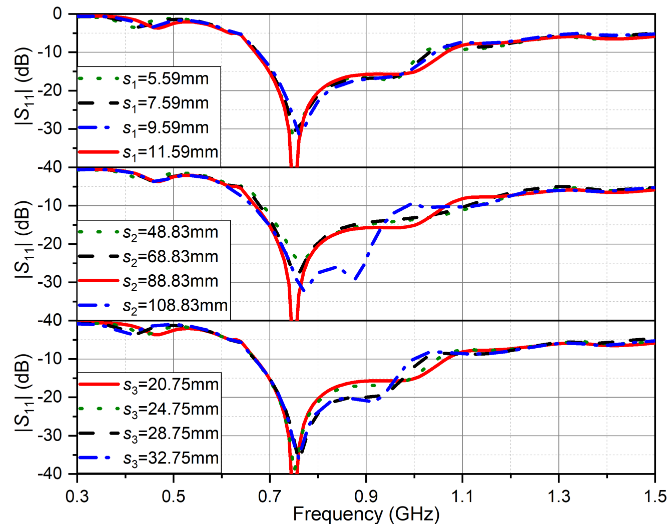

Fig. 10. Reflection coefficient of the proposed antenna versus s_1, s_2 and s_3.

With the significant reduction of the projected area of both the radiating part and the DGS, each antenna element can be independently packaged using a streamlined radome of low wind load. And the inter-radome spacing is large enough to make holes which can be used to further reduce wind load. Fluid simulations for the conceptual prototypes shown in Fig. 1 are performed in Fluent under normal temperature (298.15 K) and pressure (101.325 kPa), where the wind velocity is set as 18 m/s. Considering the industrial processes and production, the edges of each metal mesh are streamlined. The simulated pressure distribution nephograms for the traditional AAU with one radome and the novel AAU formed by the proposed antenna element are shown in Fig. 8, and the wind load is equal to the pressure integrated with respect to the projected area. According to the results given by Fluent, the wind load is reduced from 1132.79 N to 585.28 N, a 48% reduction. It can be observed that the novel AAU with small streamlined radomes has a significantly smaller projected area with higher pressure than the traditional AAU with the whole radome, which effectively reduces the wind load. Additionally, the wind load of the novel AAU can be further reduced through a better streamlined design [28]–[30].

B. Parameter Study

In this section, the influence of several key parameters, including the top angle α of bow-tie dipoles, the width of slots s_1, the length of slots s_2, the position of slots s_3 and the size of meshes a, is investigated. Since the size of the radiating part w_1 is determined, the top angle of the dipole α can be changed by adjusting the parameter h of the dipole.

Fig. 9 shows the simulated S-parameters of the proposed antenna with different top angles of the dipole α, where different α values correspond to different h. As α increases from $70.4°$ to $88.4°$, the lower resonance frequency shifts toward higher frequencies, and the higher resonance frequency shifts toward lower frequencies, improving the resonance performance. However, when α increases to $88.4°$, the proposed antenna has only one resonance frequency, worsening the impedance bandwidth. Considering the compact radiating layer, the lowest operating frequencies need to be taken seriously. Choosing $\alpha = 82.4°$ can realize a better reflection coefficient around specific operating frequencies. Additionally, when $\alpha = 82.4°$, the proposed antenna has better isolation between the two input ports.

Additionally, as shown in Fig. 10, the four intersecting square slots loaded on the defected ground layer have a substantial influence on the reflection coefficient of the proposed antenna with a small radiating part and unique reflector. As s_1 increases from 5.59 mm to 11.59 mm, the lower resonance frequency is basically unchanged, but the higher resonance frequency shifts toward higher frequencies, increasing the impedance bandwidth. As s_2 increases from 48.83 mm to 88.83 mm, the lower resonance frequency shifts to lower frequencies, making the operating frequency band move toward lower frequencies, but the higher resonance frequency also shifts downward, reducing the impedance bandwidth. As s_2 increases from 88.83 mm to 108.83 mm, the lower resonance frequency shifts higher, and the higher resonance frequency shifts downward, which reduces the impedance bandwidth and cannot meet the requirements at higher working frequencies. As s_3 increases from 20.75 mm to 32.75 mm, the lower resonance frequency remains basically unchanged, but the higher resonance frequency shifts downward, decreasing the impedance bandwidth. Considering the tradeoff between the reflection coefficient of lower working frequencies and the impedance bandwidth, all parameters of these slots should be carefully chosen to ensure the resonance performance, and parameter optimization should be utilized.

Moreover, as shown in Fig. 11, changing the size of the mesh can not only change the projected area but also have a moderate impact on the radiation performance of the proposed antenna. As a increases from 34 mm to 46 mm, the mesh area increases, and more energy is leaked, reducing the simulated realized gain and impedance bandwidth at the working frequencies. As a increases from 34 mm to 40 mm, the isolation worsens. However, when a increases from 40 mm

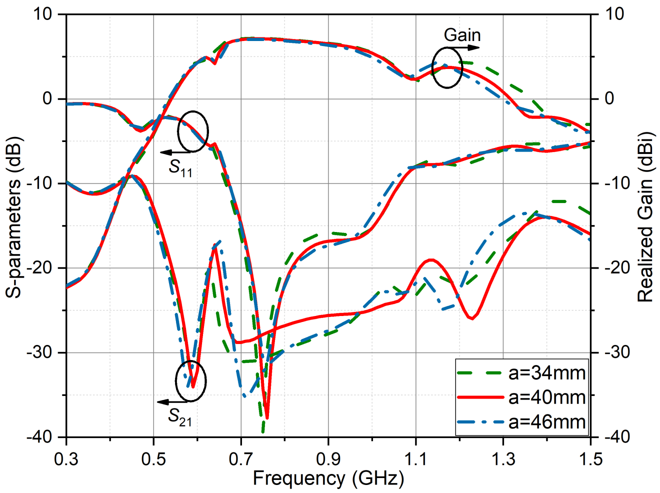

Fig. 11. S-parameters and realized gains of the proposed antenna versus a.

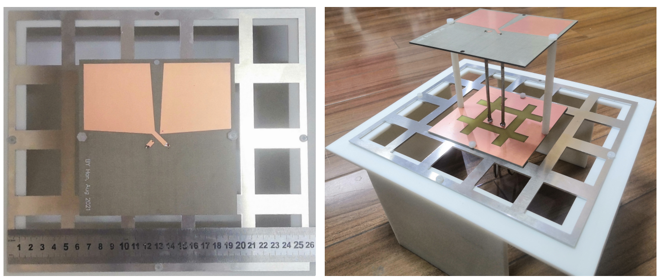

(a) (b)

Fig. 12. Photographs of (a) the top view and (b) a three-dimensional view of the proposed antenna.

to 46 mm, the isolation improves. In addition, the stability of the physical structure worsens with increasing mesh area. The change in radiation performance caused by different a is not prominent compared to the changes caused by other key parameters, but the influence of this parameter on the wind load and stable physical structure of the antenna cannot be ignored. The mesh sized $a = 40$ mm is chosen to reduce the overall projected area while maintaining structural stability and radiation performance.

III. Results and Discussion

Using the standard PCB process, an antenna prototype is fabricated for the sub-1 GHz band as an example, which is shown in Fig. 12. Two 30-cm-long flexible coaxial lines are utilized to feed the antenna. The metal mesh reflector is made of aluminum. Plastic posts, screws and nuts are used to realize physical stability. The S-parameters are measured by using a vector network analyzer, and the radiation patterns and gains are obtained in a far-field measurement system.

The simulated and measured S-parameters of the antenna prottype are shown in Fig. 13(a). The simulated and measured reflection coefficients match very well. The measured isolation between port 1 and port 2 is not as good as the simulated isolation result because of the error caused by the soldering process and transmission connector. From 680 MHz to 970 MHz, the measured S_{11} and S_{22} are lower than -10 dB, and

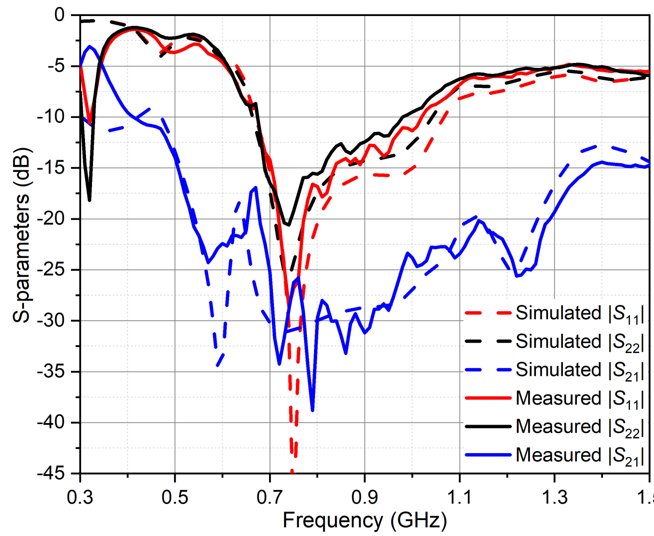

(a)

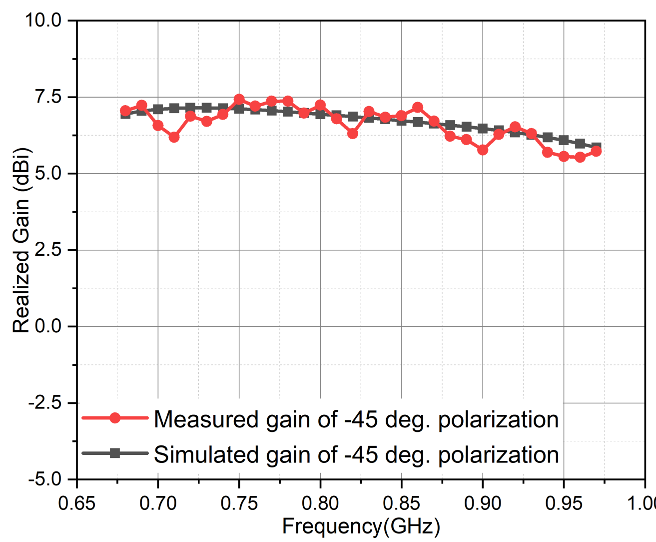

(b)

Fig. 13. Simulated and measured (a) S-parameters and (b) realized gains of the proposed antenna.

the polarization isolation is higher than 20 dB. Moreover, from 700 MHz to 970 MHz, the isolation between the two input ports is higher than 25 dB.

Within these operating frequencies, the simulated and measured gains are shown in Fig. 13(b), and the measured realized gain is 6.5 ± 1.0 dBi. The simulated and measured radiation patterns in the H-plane (xoz-plane) and V-plane (yoz-plane) for $-45°$ polarization at 680 MHz, 820 MHz and 970 MHz are described in Fig. 14. The radiation patterns for $+45°$ polarization are similar due to the symmetrical geometry. The measured radiation patterns agree with the simulated patterns, and the measured cross-polarization levels are below -18 dB in both the H- and V-planes. The above radiation performance proves that the proposed low wind load antenna with a DGS and metal mesh reflector can realize projected area reduction and simultaneously meet the requirements for 5G base stations.

A comparison between the proposed antenna and some previous designs is presented in Table II to display the

TABLE II
COMPARISON OF THE PROPOSED ANTENNA AND THOSE IN REFERENCES.

Ref.	Antenna structure	Size of the radiation part (λ_0^2)	Windward side (assuming that wind direction is parallel to the Z-axis)	Freq. (GHz)	Low wind load design
[19]	Folded dipoles with parasitic patch	0.28×0.28	Radiator and metal ground	0.825	No
[20]	ME-dipole with metamaterial loading	0.52×0.36	Radiator and metal ground	2.7	No
[23]	Band notch dipoles with AMC reflectors	0.57×0.60	Radiator and metal ground	1.8	No
[24]	Modified patch radiator fed by Y-shaped probes	0.30×0.30	Radiator and metal ground	2.6	No
This work	Printed cross dipoles with DGS	0.33×0.33	Radiator and metal mesh reflector	0.825	Yes

$\ast$ In [19], the parameters of the ground plane are not given, but the size of projected area is much larger than the size of radiation part.

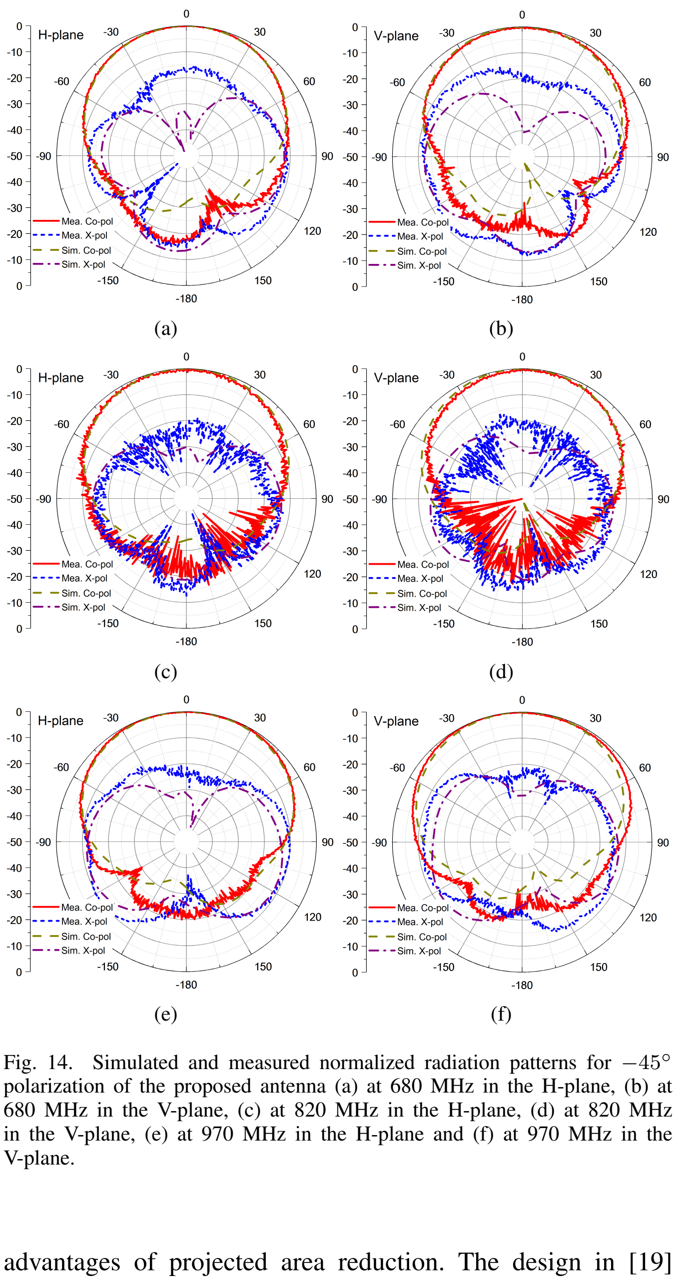

(a) (b)

(c) (d)

(e) (f)

Fig. 14. Simulated and measured normalized radiation patterns for $-45°$ polarization of the proposed antenna (a) at 680 MHz in the H-plane, (b) at 680 MHz in the V-plane, (c) at 820 MHz in the H-plane, (d) at 820 MHz in the V-plane, (e) at 970 MHz in the H-plane and (f) at 970 MHz in the V-plane.

advantages of projected area reduction. The design in [19] has a wide band and smaller radiator and can be a good candidate for integration with other antenna elements. A stable gain and a wide impedance bandwidth are realized with size reduction in [20] and [24]. A dual-band compact antenna is designed in [23], where the profile height is reduced while the antenna is miniaturized. Compared with these reported designs, the proposed antenna with emphasis on low wind load design has not only a smaller radiating part but also a small overall projected area. More significantly, the excellent broadband performance of the dual-polarized dipole antenna is still maintained.

IV. CONCLUSION

A compact cross-dipole antenna with a small radiator and overall projected area for application in 5G base stations is proposed. The size reduction of the antenna is achieved by loading a DGS and replacing the traditional intact metal ground plane with a defected ground layer and metal mesh reflector. The projected area of the radiating part and DGS is $0.33 \times 0.33\lambda_0^2$. The measured results show that the reflection coefficients are lower than -10 dB and that the isolation between two input ports is higher than 20 dB from 680 MHz to 970 MHz. Especially, from 700 MHz to 970 MHz, the isolation between the two input ports is higher than 25 dB. In addition, the realized gain is 6.5 ± 1.0 dBi and the cross-polarization levels are below -18 dB in both the H-plane and V-plane radiation patterns within operating frequencies, making the proposed antenna suitable for large-scale arrays utilized in low-wind load 5G AAUs.

REFERENCES

[1] E. Bjornson, J. Hoydis, and L. Sanguinetti, "Massive MIMO has unlimited capacity," *IEEE Trans. Wireless Commun.*, vol. 17, no. 1, pp. 574–590, 2018.

[2] M. Agiwal, A. Roy, and N. Saxena, "Next generation 5G wireless networks: A comprehensive survey," *IEEE Commun. Surveys Tuts.*, vol. 18, no. 3, pp. 1617–1655, 2016.

[3] Y. Zhu, Y. Chen, and S. Yang, "Decoupling and low-profile design of dual-band dual-polarized base station antennas using frequency-selective surface," *IEEE Trans. Antennas Propag.*, vol. 67, no. 8, pp. 5272–5281, 2019.

[4] K. W. Paper, *Base Station Antennas - Reliable Wind Load Calculation*, 2017.

[5] P. Liu, Y. Li, Z. Zhang, and Z. Feng, "Omnidirectional dual-polarized antenna with sabre-like structure," *IEEE Trans. Antennas Propag.*, vol. 65, no. 6, pp. 3221–3225, 2017.

[6] P. Liu, Z. Meng, L. Wang, Y. Zhang, and Y. Li, "Omnidirectional dual-polarized saber antenna with low wind drag," *IEEE Trans. Antennas Propag.*, vol. 68, no. 1, pp. 558–563, 2020.

[7] W. Zhang, Y. Li, Z. Zhang, and Z. Feng, "A pattern-reconfigurable aircraft antenna with low wind drag," *IEEE Trans. Antennas Propag.*, vol. 68, no. 6, pp. 4397–4405, 2020.

[8] D. Qiu, M. Sun, Z. Wang, Y. Wang, and Z. Chen, "Practical wind-disturbance rejection for large deep space observatory antenna," *IEEE Trans. Control Syst. Technol.*, vol. 22, no. 5, pp. 1983–1990, 2014.

[9] J. Zhang, J. Huang, J. Zhou, C. Wang, and Y. Zhu, "A compensator for large antennas based on pointing error estimation under a wind load," *IEEE Trans. Control Syst. Technol.*, vol. 25, no. 5, pp. 1912–1920, 2017.

[10] Y. Dong, J. Choi, and T. Itoh, "Vivaldi antenna with pattern diversity for 0.7 to 2.7 GHz cellular band applications," *IEEE Antennas Wireless Propag. Lett.*, vol. 17, no. 2, pp. 247–250, 2018.

[11] A. Gorai, M. Pal, and R. Ghatak, "A compact fractal-shaped antenna for Ultrawideband and Bluetooth wireless systems with WLAN rejection functionality," *IEEE Antennas Wireless Propag. Lett.*, vol. 16, pp. 2163–2166, 2017.

[12] M. Zeng, A. S. Andrenko, X. Liu, Z. Li, and H.-Z. Tan, "A compact fractal loop rectenna for RF energy harvesting," *IEEE Antennas Wireless Propag. Lett.*, vol. 16, pp. 2424–2427, 2017.

[13] C.-M. Luo, J.-S. Hong, and L.-L. Zhong, "Isolation enhancement of a very compact UWB-MIMO slot antenna with two defected ground structures," *IEEE Antennas Wireless Propag. Lett.*, vol. 14, pp. 1766–1769, 2015.

[14] J. Zeng and K.-M. Luk, "A simple wideband magnetoelectric dipole antenna with a defected ground structure," *IEEE Antennas Wireless Propag. Lett.*, vol. 17, no. 8, pp. 1497–1500, 2018.

[15] S. S. Jehangir and M. S. Sharawi, "A miniaturized uwb biplanar yagi-like MIMO antenna system," *IEEE Antennas Wireless Propag. Lett.*, vol. 16, pp. 2320–2323, 2017.

[16] D. E. Brocker, Z. H. Jiang, M. D. Gregory, and D. H. Werner, "Miniaturized dual-band folded patch antenna with independent band control utilizing an interdigitated slot loading," *IEEE Trans. Antennas Propag.*, vol. 65, no. 1, pp. 380–384, 2017.

[17] S.-R. Lee, E.-H. Lim, F.-L. Bong, and B.-K. Chung, "Slotted folded patch antenna with double-T-slots for platform-insensitive UHF tag design," *IEEE Trans. Antennas Propag.*, vol. 67, no. 1, pp. 670–675, 2019.

[18] W. Hu, X. Liu, S. Gao, L. Wen, Q. Luo, P. Fei, Y. Yin, and Y. Liu, "Compact wideband folded dipole antenna with multi-resonant modes," *IEEE Trans. Antennas Propag.*, vol. 67, no. 11, pp. 6789–6799, 2019.

[19] J.-H. Ou, Z. Chen, S. F. Bo, Y. Zhang, and X. Y. Zhang, "Compact dual-polarized antenna with low-pass response for marine communication," *IEEE Trans. Veh. Technol.*, vol. 70, no. 3, pp. 2649–2656, 2021.

[20] M. Li, K.-M. Luk, L. Ge, and K. Zhang, "Miniaturization of magnetoelectric dipole antenna by using metamaterial loading," *IEEE Trans. Antennas Propag.*, vol. 64, no. 11, pp. 4914–4918, 2016.

[21] S. Ahdi Rezaeieh, M. A. Antoniades, and A. M. Abbosh, "Miniaturization of planar Yagi antennas using Mu-negative metamaterial-loaded reflector," *IEEE Trans. Antennas Propag.*, vol. 65, no. 12, pp. 6827–6837, 2017.

[22] M. Zada, I. A. Shah, and H. Yoo, "Metamaterial-loaded compact high-gain dual-band circularly polarized implantable antenna system for multiple biomedical applications," *IEEE Trans. Antennas Propag.*, vol. 68, no. 2, pp. 1140–1144, 2020.

[23] M. Li, Q. Li, B. Wang, C. Zhou, and S. Cheung, "A miniaturized dual-band base station array antenna using band notch dipole antenna elements and AMC reflectors," *IEEE Trans. Antennas Propag.*, vol. 66, no. 6, pp. 3189–3194, 2018.

[24] Y. Chen, C. Zhang, Y. Lu, W.-W. Yang, and J. Huang, "Compact dual-polarized base station antenna array using laser direct structuring technique," *IEEE Antennas Wireless Propag. Lett.*, vol. 20, no. 1, pp. 78–82, 2021.

[25] B. Han, Q. Wu, H. Wang, and X. Gao, "Ultra-compact dual-polarized dipole antenna for ultra-massive mimo systems," in *2021 IEEE/CIC Int. Conf. on Commun. China (ICCC Workshops)*, 2021, pp. 395–398.

[26] M. Sanad and N. Hassan, "A low wind-load lightweight foldable/deployable multi-beam base station antenna for the whole LTE spectrum," in *2018 Wireless Days (WD)*. IEEE, 2018, pp. 31–33.

[27] Y. Cui, R. Li, and H. Fu, "A broadband dual-polarized planar antenna for 2G/3G/LTE base stations," *IEEE Trans. Antennas Propag.*, vol. 62, no. 9, pp. 4836–4840, 2014.

[28] C. Scruton, C. W. Newberry, and BRS, "On the estimation of wind loads for building and structural design." *Proceedings of the Institution of Civil Engineers*, vol. 25, no. 2, pp. 97–126, 1963.

[29] Y. Zhang, H. Hu, and P. P. Sarkar, "Comparison of microburst-wind loads on low-rise structures of various geometric shapes," *Journal of Wind Engineering and Industrial Aerodynamics*, vol. 133, pp. 181–190, 2014.

[30] I. M. V. Andersen, "Wind loads on post-panamax container ship," *Ocean engineering*, vol. 58, pp. 115–134, 2013.